

Distinguishing between renal oncocytoma and chromophobe renal cell carcinoma using Raman molecular imaging

Shona Stewart,^{a*} Heather Kirschner,^a Patrick J. Treado,^a Ryan Priore,^b Maria Tretiakova^c and Jeffrey K. Cohen^d



Raman molecular imaging was evaluated as a tool for differentiating between kidney tumors which are sometimes confused using conventional histopathological methods.

Renal oncocytoma and chromophobe renal cell carcinoma are two kidney tumors which occasionally possess overlapping histological features. There is no reliable alternative method to routine histologic examination for differentiating these neoplasms. However, a conclusive diagnosis is important, as renal oncocytoma is benign and chromophobe renal cell carcinoma has malignant potential, requiring different treatment options.

In an investigation based on 88 patients, a partial least squares discriminant analysis model generated from Raman molecular images distinguished between chromophobe renal cell carcinoma and renal oncocytoma with a performance of 86% sensitivity and 81% specificity.

These initial observations suggest that Raman molecular imaging may be applied not only to the differentiation of these kidney tumors but also to other applications for which conventional histological methods are not sufficient for a conclusive diagnosis. Copyright © 2014 John Wiley & Sons, Ltd.

Additional supporting information may be found in the online version of this article at the publisher's web site.

Keywords: chromophobe; oncocytoma; kidney cancer; Raman imaging; PLS-DA

Introduction

The use of digital technology in disease diagnosis is currently making a significant impact in medicine. Amongst the emerging digital technologies, Raman imaging techniques promise rapid analysis of tissue without the use of additional reagents or staining.

Raman spectroscopy is routinely employed as an analytical tool in a variety of industries such as pharmaceuticals and polymer manufacturing. The technology has also been applied to cells and tissues, is potentially capable of being employed *in vivo*, and in recent studies has shown promise in identifying disease progression. These applications, in addition to molecular-level specificity and sample preparation without reagents, make Raman technology an appealing addition to the more conventional analysis methods used in medicine today. Raman spectroscopy has been evaluated as a diagnostic tool for a large number of medical applications. It has been applied to cancer and precancer diagnosis and detection in a variety of organs such as breast,^[1,2] esophagus,^[3] cervix,^[4] oral cavity,^[5] stomach,^[6] skin,^[7] prostate,^[8,9] colon,^[10] kidney,^[11–13] and brain.^[14] The majority of these investigations has focused on identifying the presence^[1,2,7,10–14] or early detection^[3–6] of disease in humans. *In vivo* Raman measurements have been demonstrated in a number of reports.^[11,12] In many cases, diagnostic sensitivity and specificity are high. For example, Lyng and coworkers obtained 98.5% sensitivity and 99% specificity for the identification of invasive cervical carcinoma.^[4] Furthermore, Raman sampling is versatile enough for application to both fresh tissues and formalin-fixed paraffin-embedded (FFPE) tissues.

Evidence that Raman spectral features can be correlated with molecular composition and structure associated with the disease state of a tissue is convincing. Raman molecular imaging (RMI) combines the sensitivity and specificity of Raman spectroscopy with digital imaging technology, yielding a methodology for visualizing both the morphological and chemical compositions of a material simultaneously.^[15] RMI offers the ease of interpretation

* Correspondence to: Shona Stewart, ChemImage Corporation, 7301 Penn Avenue, Pittsburgh, PA 15208, USA.
E-mail: sstewart@chemimage.com

a ChemImage Corporation, 7301 Penn Avenue, Pittsburgh, PA, 15208, USA

b Cirtemo™, 618 Naples Avenue, Columbia, SC, 29033-4011, USA

c University of Washington Medical Center, 1959 NE Pacific St, Seattle, WA, 98195, USA

d Division of Urology, Allegheny General Hospital, Federal North Building, 1307 Federal Street, Suite 300, Pittsburgh, PA, 15212, USA

Nonstandard abbreviations: RMI, Raman molecular imaging; FOV, Field of view; ChRCC, Chromophobe renal cell carcinoma; ONC, Renal oncocytoma; ROI, Region of interest; MCF, Multiconjugate filter; CIXpert, ChemImage Xpert™; NIST, National Institute of Standards and Technology; PCA, Principal component analysis; MD, Mahalanobis distance; PLS-DA, Partial least squares discriminant analysis; NIR, Near infrared; ROC, Receiver operator characteristic; AUROC, Area under the receiver operator characteristic; FFPE, Formalin-fixed paraffin-embedded; TME, Tissue microarray; RGB, Red Green Blue – used to refer to color imagery with a video camera.

of a digital imaging method with the high molecular specificity of Raman measurements.

One particularly challenging problem for pathologists is differentiating between two specific kidney neoplasms. Chromophobe renal cell carcinoma (ChRCC) is a subtype of renal cell carcinoma which comprises approximately 5% of all renal tumors.^[16] Renal oncocytoma (ONC) is a common benign neoplasm, characterized by large numbers of mitochondria in its granular cytoplasm.^[17] In the eosinophilic form, ChRCC tumor cells also have a granular cytoplasm which resembles that of ONC tumor cells but are composed of cytoplasmic microvesicles and abnormal mitochondria. As a result, the two neoplasms can have overlapping histological features. The 'gold standard' method for identifying ChRCC is histological examination. A number of special stains and immunohistochemical markers, such as Hale's colloidal iron stain, have been employed to differentiate ChRCC from ONC. However, none of these is substantially specific to either tumor type,^[18,19] and some can be technically challenging to perform, with results which are difficult to interpret.^[20] In cases where ChRCC cannot be histologically distinguished from ONC, a patient will be treated as if there were a malignancy, resulting in more aggressive or invasive treatment than may be necessary. A method to distinguish between ONC and ChRCC in cases of histological overlap would conceivably reduce the number of unnecessary surgeries.

This study evaluates RMI for distinguishing between ChRCC and ONC on conventional FFPE tissues. A technique which can be used to assist in diagnosis of ONC and ChRCC would have an invaluable impact on the physical and emotional welfare of patients, in addition to reducing the burden of decision faced by clinicians.

Materials and methods

Tissues

ONC and ChRCC tissue sections were provided by two sources. Conventional histological tissue sections from 20 patients diagnosed with ONC and 14 patients diagnosed with ChRCC were provided by the Allegheny General Hospital (Pittsburgh, PA) Pathology Department. Tissue microarray (TMA) sections from 17 patients diagnosed with ONC, 37 patients diagnosed with ChRCC, and 9 patients diagnosed as normal were obtained from the University of Chicago Medical Center (Chicago, IL) Department of Pathology. Many of these latter tissue sections were obtained in replicate and triplicate. All samples were obtained under appropriate Institutional Review Board (IRB) regulations.

Tissues were sectioned into 4- μm -thick slices from paraffin blocks. For each tissue, adjacent sections were placed on both glass and aluminum-coated microscope slides. Tissue sections on glass slides were stained with hematoxylin and eosin (H & E) for histopathological examination, while tissue sections for Raman experiments were placed on aluminum-coated slides, deparaffinized and left without a cover slip.

Raman molecular imaging

Raman molecular images were generated on a FALCON II™ Wide-Field Raman Chemical Imaging System (ChemImage Corp., Pittsburgh, PA). A Nd:YAG laser lasing at 532 nm was utilized for excitation, and a Multi-conjugate filter (MCF, ChemImage, Corp., Pittsburgh, PA) was employed as the imaging spectrometer.

The excitation light was directed through a 50 \times microscope objective to the tissue sample, then the Raman scattered light was directed back through the microscope to an electron multiplying charge-coupled device (EMCCD, Andor Technology, South Windsor, CT), which detected the Raman photons with a spectral resolution of 9 cm^{-1} FWHM. This mode of image collection is also known as wide-field or hyperspectral imaging. Brightfield (i.e. RGB) images of unstained and H & E stained tissues were collected using a $\mu\text{Eye}^{\circledR}$ 1460-C video camera (Imaging Development Systems, Obersulm, Germany) housed on the Falcon II system. Instrument control and data processing were performed with commercially available software programs, ChemImage Xpert™ (CIXpert, ChemImage, Corp., Pittsburgh, PA) and MATLAB® (Mathworks, Natick, MA).

Raman molecular images were collected over the range 600–3200 cm^{-1} at high spectral resolution, resulting in a total of 391 frames (or Raman shifts) in each image. At each Raman shift, the tissue was exposed to the laser at a power of 100 mW for 9 s. Over each sample field of view (FOV), the laser power density was 5669 Wcm^{-2} . A dark current contribution was measured in advance and subtracted from the images as they were acquired. Raman molecular images from several adjacent FOVs at 50 \times magnification were digitally concatenated to create larger regions of interest (ROI) ranging between 120 $\mu\text{m} \times 120 \mu\text{m}$ and 200 $\mu\text{m} \times 200 \mu\text{m}$.

Experimental methodology

For each tissue section imaged, the following steps were performed:

- Regions of tumor cells were identified on the H & E stained tissue. For conventional histological sections, these regions were identified by a pathologist. In some cases, the unstained tissue was stained with H & E post-Raman image acquisition.
- The corresponding area on the unstained adjacent tissue section was located.
- Brightfield images of both ROIs were collected.
- Raman molecular images of the unstained tissue were collected and processed.
- The Raman molecular image was 'fused' digitally to either the brightfield image of the same ROI after H & E staining or the brightfield image of the corresponding location on the H & E stained adjacent tissue section. Digital fusion of images matches tissue features visible in a brightfield image with spectral data corresponding to the same features in the Raman molecular image.
- Regions of tumor cells within the stained brightfield image were selected, enabling the extraction of Raman image spectra from the fused Raman molecular image.
- Extracted Raman image spectra were processed and analyzed using chemometric methods.

Data preprocessing

Raman molecular images were processed post-acquisition to correct for cosmic events, instrument response, and illumination uniformity. Cosmic events were removed using a 5 \times 5 median kernel filter. Pixel intensities that varied more than 3 standard deviations from the average intensity within the kernel were replaced with the median intensity of the kernel. A standard reference material with a known Raman response at 532 nm laser

excitation (Standard Reference Material 2242), developed by the National Institute of Standards and Technology (NIST, Gaithersburg, MD), was utilized to correct for instrument response and slight illumination irregularities across the tissue.

For each case, 2 to 15 Raman image spectra were extracted. In total, the cases are represented by 354 ONC and 774 ChRCC image spectra. After spectral truncation to 860–1860 cm^{-1} , image spectra were baseline adjusted using a first order polynomial fit, then vector normalized. A calibration transfer was applied to all extracted image spectra to take into account the non-linear spectral shift existing between data populations due to differences in the instruments over the time period of the project. This spectral alignment was performed by applying a piecewise linear correction using four known peaks occurring in tissue to shift and stretch the spectra: 1002 cm^{-1} , 1035 cm^{-1} , 1450 cm^{-1} , and 1672 cm^{-1} .

Data analysis

Partial least squares discriminant analysis (PLS-DA) is a well-known statistical method of analysis and has been explained previously for data reduction, model creation, and data classification. Briefly, it is a supervised classification method often employed to differentiate between known classes, with the goal of using the resulting PLS-DA model to predict the class membership for unknown observations.^[21,22] PLS-DA was employed to create a two-class model describing the relationship between ONC and ChRCC image spectra and provide a means of predicting the class membership of unknown cases. A leave-one-out cross-validation (LOO-CV) technique was employed to validate the model. In this method, the PLS-DA model is built repeatedly, each time leaving out the spectral data of one case, until the image spectra corresponding to all cases have been tested.

Performance of the model is assessed through a receiver operator characteristic (ROC) curve analysis. An ROC curve is a plot showing sensitivity *versus* 1-specificity of a test for a binary system. This technique of performance evaluation is used as a tool to select an optimal threshold of a data set that maximizes sensitivity and specificity. It is generated by calculating a PLS-DA score for each case from the measured spectroscopic data followed by sweeping a threshold value across the observed score values. The true positive, true negative, false positive, and false negative detections as compared to a ground truth are calculated at each threshold value to yield the sensitivity and specificity results. The area under the ROC curve (AUROC) is a measure that is often used to compare performance of ROC curves with a single value. The area under a perfect ROC curve is 1.

Another way to exploit the mode of wide-field imaging is the ability to apply a 'digital stain' to a Raman molecular image. In this technique, the generated PLS-DA model is used to classify every pixel in a Raman image as either ChRCC or ONC. When digitally staining a Raman image as ChRCC, the pixels have values from 0 to 1 representing a score for ChRCC, where 1 is the highest score, and 0 is the lowest. Pixels scoring 1 are white, and those scoring 0 are black. Therefore, a digitally stained Raman molecular image of a known ChRCC will appear to be brighter when classifying for ChRCC than when classifying for ONC.

Results and discussion

Raman molecular imaging and image spectra

To our knowledge, only one report of RMI (i.e. in wide-field mode) for disease diagnosis has been published.^[9] The unique nature of

this study lies in the mode of Raman imaging and the use of FFPE tissue sections. The ability to collect Raman data from paraffin-embedded tissues increases the utility of RMI since FFPE tissues are readily available in tissue banks; they archive safely, and in most cases, provide enough tissue for preparing multiple sections if necessary.

A number of methodologies exist for Raman imaging techniques for cells and tissues^[7,14,23–28]; however, these are mapping techniques which can suffer technical drawbacks not observed when collecting Raman molecular images with a wide-field methodology. Long acquisition times are a possibility with mapping, due to the need for collecting a single Raman spectrum at very small intervals across an ROI. Subsequent to the large time interval between acquisition of spectra at the first and final locations is the potential for background influences to be non-uniform across the data set and therefore difficult to remove.

In contrast to images collected by mapping methods, high-definition Raman molecular images are collected in a time-efficient manner by selecting discrete Raman spectral ranges as a function of time, capturing an image of a whole FOV with each CCD camera integration. The collection of Raman information of all points in a FOV reduces non-uniformity of background factors. Furthermore, because data is collected over discrete free spectral ranges, the total acquisition time can be minimized by the user.

To produce Raman molecular images and spectra, Raman scattered light from the sample passes through the MCF, which is electronically tuned to allow throughput of the light at discrete wavelengths or Raman shifts before being imaged by the detector. Each image frame contains Raman information from every pixel in the FOV. Hence, both spatial and molecular information is collected simultaneously. Consequently, each pixel within an image contains Raman spectral information, and observing a single pixel over the complete set of image frames yields a Raman spectrum that describes the molecular composition of the sample in the pixel location. Spectral differences ultimately provide the contrast in the Raman image. This enables the conversion of a virtually featureless brightfield image into an image showing high contrast, which may be colored to show regions of differing spectral information.

The benefits of Raman contrast are illustrated by comparing a typical brightfield reflectance image of a stained kidney tissue section (Fig. 1(a)) with a snapshot of the corresponding three-dimensional Raman molecular image of the tissue section (Fig. 1(b)), which comprises 391 frames, each representing Raman scattered light at a different wavelength. Digital fusion of the Raman image to the brightfield image enables a pathologist to identify regions in a conventionally stained tissue section (Fig. 1(a)) in order to yield Raman data describing the selected tumor cells (Fig. 1(c)).

Because the majority of biological tissues are composed of proteins, lipids, carbohydrates, and nuclear material, Raman spectra of tissues exhibit a degree of similarity. The average of the 354 ONC and 774 ChRCC image spectra shows subtle spectral differences (Fig. 2). Peaks at 1002, 1035, 1120, 1316, 1336, 1450, 1612, and 1672 cm^{-1} represent the major components in the kidney tissue. These are typical Raman peaks in biological spectra and have previously been attributed to the phenylalanine ring breathing mode, phenylalanine CH ring bending mode, CC stretching mode in lipids, CH wagging mode (both 1316 and 1336 cm^{-1}), CH deformation mode, CC in-plane bending mode of phenylalanine and tyrosine, and the C=O stretching mode of Amide I, respectively.^[6,29,30] This is summarized in the table in Fig. 2. The most significant differences between the

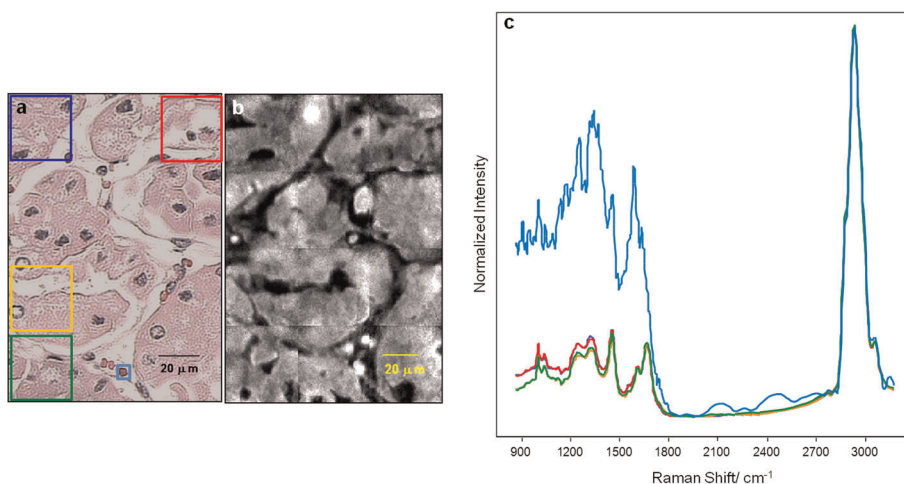


Figure 1. Typical Raman molecular image and image spectra. (a) Brightfield image of a tissue section prepared for histological examination. (b) Raman image of adjacent tissue section, unstained. (c) Extracted Raman image spectra representing highlighted cells of interest.

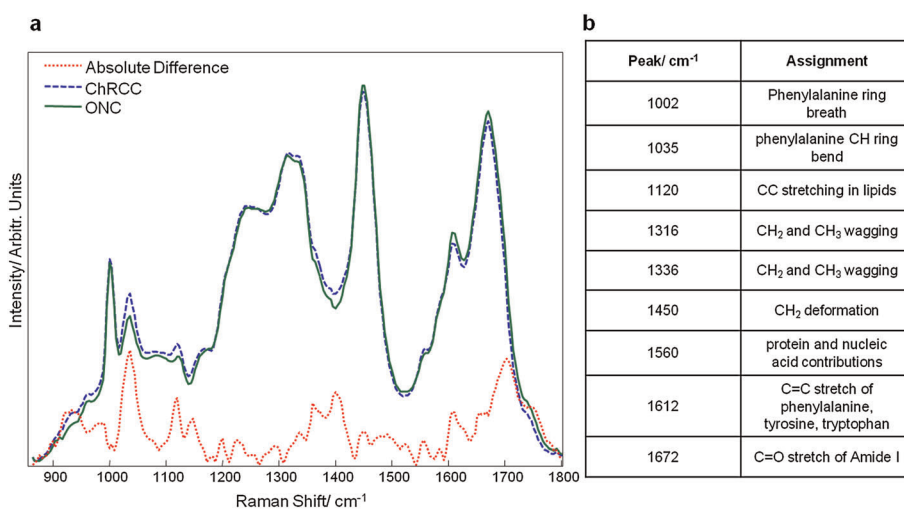


Figure 2. Average image spectra of ChRCC (dashed line) tumor cells, ONC (solid line) tumor cells, and the difference spectrum (dotted line). Table shows peak assignments.

ONC and ChRCC average spectra are at 1035, 1120, and 1612 cm⁻¹. A smaller difference between the two average spectra can be seen at 1560 cm⁻¹. These spectral distinctions are highlighted in a difference spectrum between the two averages (Fig. 2).

Differentiation between the two neoplasms was made possible because of the ability to extract data exclusive to ONC and ChRCC cells from Raman molecular images and thus eliminate background interferences. Selection of the tumor cells and exclusion of the background elements ensures that the Raman signal is representative of the cells of interest only. This is illustrated in Fig. 1. The light blue highlighted region (not used in the analysis) yields a spectrum with significantly different peak positions as compared to the other image spectra in the figure. This artifact is in fact a red blood cell, whose spectral presence is not only unnecessary for analysis of ChRCC and ONC, but it would also skew the results. This demonstration of the versatility of RMI and the benefit of pixel-specific spectral information makes RMI a preferred method for tissue diagnosis.

Model creation and validation

The use of multivariate statistical methods for analyzing image data is becoming more common.^[7,9,24,31,32] In previous, unpublished work, we found that PLS-DA demonstrated higher accuracy than other multivariate statistical analyses when classifying test data.

A PLS-DA model was built using LOO-CV of 354 ONC and 774 ChRCC image spectra representing 37 ONC and 51 ChRCC patients. The spectral region between 860 and 1860 cm⁻¹ was employed for data analysis. Eight factors were found to be significant to this analysis. The variance of the x- and y-blocks is explained by 99.7% and 83.4% of the ChRCC data, respectively, and by 99.7% and 63.5% of the ONC data, respectively. Figure 3 (a) illustrates the discriminant plot for the eight-factor PLS-DA model. The ROC curve illustrating the performance of the model (Fig. 3(b)) has an AUROC of 0.87. Sensitivity of the model as a test for the malignant ChRCC condition is 86% and specificity is 81%. This is also illustrated in the discriminant plot (Fig. 3(a)) by the dashed line, which corresponds to a threshold producing 86%

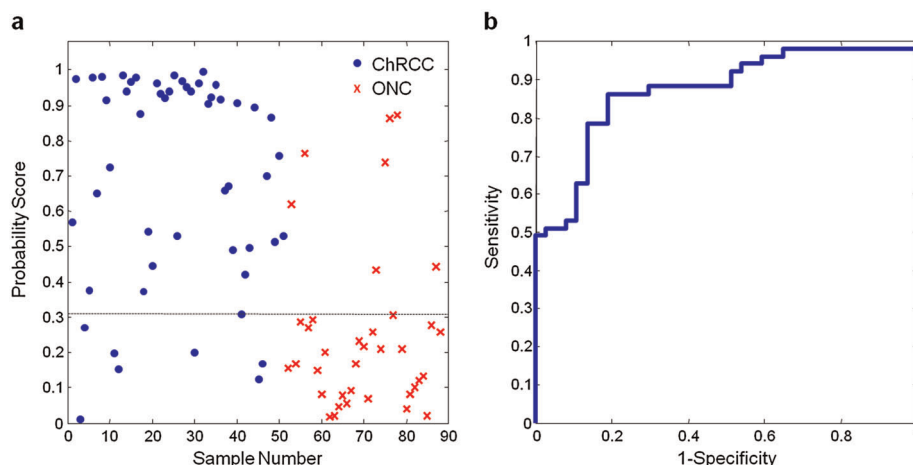


Figure 3. Evaluation of an eight-factor PLS-DA model. (a) Discriminant plot and (b) ROC curve with an AUROC of 0.87, illustrating model performance.

sensitivity and 81% specificity. Compared to the commonly utilized Cytokeratin 7 (CK7) IHC test for distinguishing ChRCC and ONC, the performance of RMI is higher in specificity and lower in sensitivity.^[33] Seven ChRCC cases and seven ONC cases were identified as outliers of the model (i.e. outside the threshold of each class). Assessment of image spectra corresponding to these cases revealed no evidence suggesting correlation between the outliers.

A critical parameter when building the PLS-DA model is the number of factors retained, as each factor sequentially describes less important variance within the data set. It is possible to overfit the spectroscopic data by modeling noise through the retention of excessive PLS factors. In this study, three plots were used as guidance when selecting the number of factors for a specific model. The PLS-DA model is built repeatedly, varying the number of factors retained to generate the three plots. The plots in Figs. S1(a) and S1(b) (Supporting Information) illustrate the effect of number of factors on the ROC curve of the test. Too few factors do not describe the data accurately; using too many factors can result in fitting noise to the model, which causes model inaccuracies. The first plot, shown in Fig. S1(a), displays the misclassification rate of the model with a specific number of factors retained. This plot is created by assuming a case is assigned to the class with the higher probability. In the final model, cases are assigned to a class based on a threshold chosen from the ROC curve. The second plot (Fig S1(b)) compares the number of factors retained with one minus the AUROC. The ROC curve with the greatest AUROC does not always produce the highest sensitivity and specificity pair. For each number of factors, a new ROC curve is generated, and the optimal operating point on each ROC curve is determined as the point on the ROC curve closest to an ideal sensor (i.e. 100% sensitivity, 100% specificity). The ROC curve whose optimal operating point is closest to an ideal sensor determines the number of factors employed. The three plots are considered when choosing the number of factors to use for each model. In the case of this study, and as indicated in Fig S1(a), the optimum number of factors is 8.

Another PLS-DA model, generated from normal kidney, ONC, and ChRCC, was compared to the two-class model discriminating between the two cancers. To build the three-class model, data from nine normal kidney cases were added to the 88 ONC and ChRCC data sets. LOO-CV was employed to create this model. A test for ChRCC (vs a class including normal and ONC case data) using seven factors yielded a ROC curve with an area

under the curve of 0.88. The analysis also yielded 82% sensitivity and 87% specificity.

Adding a small population of normal kidneys to the data set improved the performance of the model. A PLS-DA model was built with seven factors as a test for ChRCC, using Raman data from normal, ONC and ChRCC cases as test spectra. Although the results favor our model, we must take into consideration the very small number of normal kidney data points compared to data corresponding to the tumor cases. Another factor to take into consideration is that in a pathology laboratory, a test for ONC and ChRCC would be the test required; normal kidney would have been diagnosed by the pathologist. Nevertheless, the performance of the model containing normal kidney image spectra is promising, with a sensitivity of 82% and specificity of 87%.

Digital 'staining' of a Raman molecular image for class prediction of a neoplasm is illustrated in Fig. 4. A known ChRCC is classified for both ChRCC and ONC with digital staining. Figure 4 (a) shows the H & E stained image of the ROI, and Fig. 4(b) is the corresponding Raman molecular image. Figure 4(c) shows the Raman molecular image after digital staining for ONC, and Fig. 4 (d) shows the Raman molecular image after digital staining for ChRCC. The mean ONC score is 0.45, and the mean ChRCC score is 0.77, correctly classifying this tissue as ChRCC.

Our results show that digital imaging in combination with Raman spectroscopy can overcome the limitations sometimes experienced when using staining methods. Discrimination of ONC and ChRCC by RMI is achieved specifically because of features unique to RMI. The chemical specificity of Raman spectroscopy allows the detection of molecular differences between ONC and ChRCC. The most significant spectral difference between average ONC and ChRCC image spectra is the peak at 1035 cm^{-1} , corresponding to the phenylalanine ring bend mode. Spectral evidence suggests that chromophobes have a higher phenylalanine content than oncocytomas. To our knowledge, there is no biological evidence suggesting this phenomenon. The broad envelope peaking at 1672 cm^{-1} is recognized as representative primarily of the C=O stretching mode of the Amide I bond in proteins.^[2,26,34,35] The peak at 1612 cm^{-1} exhibits shape and characteristics of that previously assigned to the CC in-plane bending mode of tyrosine and phenylalanine.^[29,36] Both peaks have been associated with the Raman spectrum of mitochondria.^[28,37] Comparison of average ONC and ChRCC image spectra shows that both peaks are more intense in the ONC spectrum (Fig. 3). This finding supports the fact that ONC cells are known to contain higher levels of mitochondria in the cytoplasm.^[17]

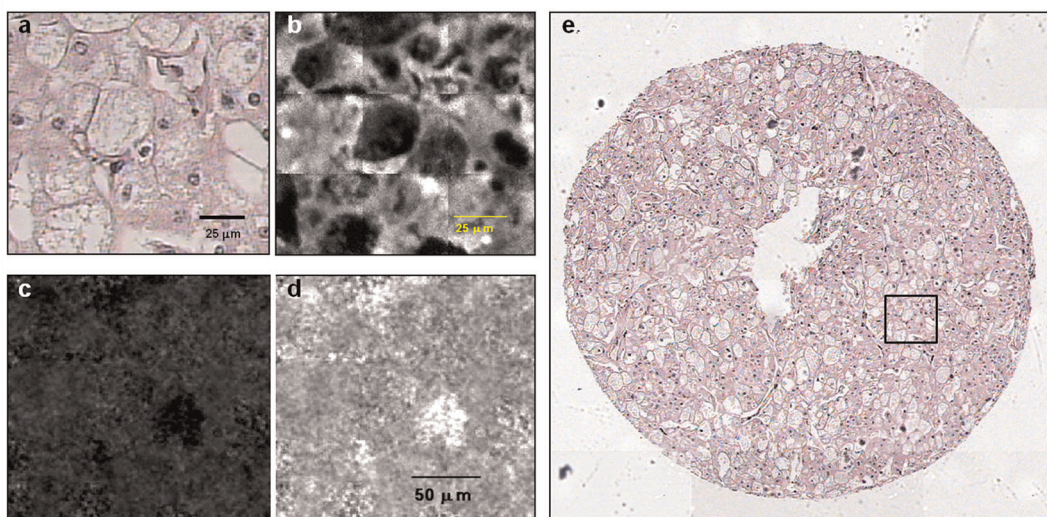


Figure 4. Digital 'staining' of Raman molecular images using the PLS-DA model. (a) Brightfield image of stained known chromophobe; (b) Raman molecular image of same ROI; (c) Raman image digitally stained for ONC; (d) Raman image digitally stained for ChrCC; (e) entire TMA section stained with H & E.

Conclusions

When a tissue biopsy is not conclusive based upon histopathological techniques, a pathologist may turn to ancillary tests to make a more specific diagnosis. In the difficult differential diagnosis of ChrCC versus ONC, a reliable test to distinguish these two kidney neoplasms is necessary. The positive results obtained in this study are significant. Not only can RMI assist pathologists in difficult cases of ONC and ChrCC, it is evident that this technology has a place in the pathology laboratory for other cases which may prove histologically difficult to diagnose.

Acknowledgements

The authors wish to acknowledge the support of the Western Pennsylvania Prostate Cancer Foundation. We would also like to thank Dr John Maier, Dr Jan Silverman, and Dr Peter Olson for their guidance in parts of this project, and Dr Arlette Uihlein for her assistance in obtaining initial samples.

Conflict of interest

Shona Stewart, Heather Kirschner, and Patrick J. Treado are employees of ChemImage Corporation.

References

- [1] M. V. P. Chowdary, K. K. Kumar, J. Kurien, S. Matthew, C. M. Krishna, *Biopolymers* **2006**, *83*, 556.
- [2] J. S. Thakur, H. Dai, G. K. Serhatkulu, R. Naik, V. M. Naik, A. Cao, A. Pandya, G. W. Auner, R. Rabah, M. D. Klein, C. Freeman, *J. Raman Spectrosc.* **2007**, *38*, 127.
- [3] G. Shetty, C. Kendall, N. Shepherd, N. Stone, H. Barr, *Br. J. Cancer* **2006**, *94*, 1460.
- [4] F. M. Lyng, E. O. Faolain, J. Conroy, A. D. Meade, P. Knief, B. Duffy, M. B. Hunter, J. M. Byrne, P. Kelehan, H. J. Byrne, *Exp. Mol. Pathol.* **2007**, *82*, 121.
- [5] R. Malini, K. Venkatakrishna, J. Kurien, K. M. Pai, L. Rao, V. B. Kartha, C. M. Krishna, *Biopolymers* **2006**, *81*, 179.
- [6] S. K. Teh, W. Zheng, K. Y. Ho, M. Teh, K. G. Yeoh, Z. Huang, *Br. J. Cancer* **2008**, *98*, 457.
- [7] A. Nijssen, T. C. Bakker Schut, F. Heule, P. J. Caspers, D. P. Hayes, M. H. Neumann, G. J. Puppels, *J. Invest. Dermatol.* **2002**, *119*, 64.
- [8] P. Crow, B. Barrass, C. Kendall, M. Hart-Prieto, M. Wright, R. Persad, N. Stone, *Br. J. Cancer* **2005**, *92*, 2166.
- [9] M. Tollefson, J. Magera, T. Sebo, J. Cohen, A. Drauch, J. Maier, I. Frank, *BJU Int.* **2010**, *106*, 484.
- [10] M. V. P. Chowdary, K. K. Kumar, K. Thakur, A. Anand, J. Kurien, C. M. Krishna, S. Matthew, *Photomed. Laser Surg.* **2007**, *25*, 269.
- [11] K. Bensalah, J. Fleureau, D. Rolland, O. Lavastre, N. Rioux-Leclercq, F. Guillé, J.-J. Patard, L. Senhadji, R. de Crevoisier, *Eur. Urol.* **2010**, *58*, 602.
- [12] J. Fleureau, K. Bensalah, D. Rolland, O. Lavastre, N. Rioux-Leclercq, F. Guillé, J.-J. Patard, R. de Crevoisier, L. Senhadji, *Expert Syst. Appl.* **2011**, *38*, 14301.
- [13] C. A. Lieber, M. H. Kabeer, *J. Pediatr. Surg.* **2010**, *45*, 549.
- [14] C. Krafft, S. B. Sobottka, G. Schackert, R. Salzer, *Analyst* **2005**, *130*, 1070.
- [15] S. Stewart, R. J. Priore, M. P. Nelson, P. J. Treado, *Annu. Rev. Anal. Chem.* **2012**, *5*, 337.
- [16] P. Dal Cin, in *Atlas of Genetic and Cytogenetic Oncology and Haematology* (Ed.: J.-L. Huret), **2001**. <http://AtlasGeneticsOncology.org/Genes/ChromophobeRenalID5124.html> (accessed 20 February 2009).
- [17] E. Garcia, M. Li, *Am. J. Clin. Pathol.* **2006**, *125*, 392.
- [18] M. V. Yusenko, *Int. J. Urol.* **2010**, *17*, 602.
- [19] M. V. Yusenko, *Int. J. Urol.* **2010**, *17*, 592.
- [20] H.-Y. Wang, S. E. Mills, *Am. J. Surg. Pathol.* **2005**, *29*, 640.
- [21] H. Martens, T. Naes, *Multivariate calibration*, John Wiley & Sons, New York, **1989**.
- [22] M. Barker, W. Rayens, *J. Chemometr.* **2003**, *17*, 166.
- [23] J. Timlin, A. Carden, M. D. Morris, R. M. Rajachar, D. H. Kohn, *Anal. Chem.* **2000**, *72*, 2229.
- [24] C. Krafft, T. Knetschke, A. Siegner, R. H. W. Funk, R. Salzer, *Vib. Spectrosc.* **2003**, *32*, 75.
- [25] N. Uzunbajakava, A. Lenferink, Y. Kraan, B. Willekens, G. Vrensen, J. Greve, C. Otto, *Biopolymers* **2003**, *72*, 1.
- [26] C. Creely, B. Volpe, G. Singh, M. Soler, D. Petrov, *Opt. Express* **2005**, *13*, 6105.
- [27] C. Matthaus, T. Chemenko, J. Newmark, C. M. Warner, M. Diem, *Biophys. J.* **2007**, *93*, 668.
- [28] Y. Naito, A. Toh-e, H.-O. Hamaguchi, *J. Raman Spectrosc.* **2005**, *36*, 837.
- [29] N. Stone, C. Kendall, N. Shepherd, P. Crow, H. Barr, *J. Raman Spectrosc.* **2002**, *33*, 564.
- [30] K. M. Omberg, J. C. Osborn, S. L. Zhang, J. P. Freyer, J. R. Mourant, J. R. Schoonover, *Appl. Spectrosc.* **2002**, *56*, 813.
- [31] A. Tripathi, R. E. Jabbar, P. J. Treado, J. H. Neiss, M. P. Nelson, J. L. Jensen, A. P. Snyder, *Appl. Spectrosc.* **2008**, *62*, 1.

- [32] C. Eliasson, A. Loren, J. Engelbretsson, M. Josefson, J. Abrahamsson, K. Abrahamsson, *Spectrochim. Acta, Part A* **2005**, *61*, 755.
- [33] M. Tretiakova, S. Stewart, J. Maier, United States and Canadian Academy of Pathology Annual Meeting, San Antonio, TX, USA, **2011**.
- [34] W. Herrebout, K. Clou, H. O. Desseyn, N. Bleton, *Spectrochim. Acta, Part A* **2003**, *59*, 47.
- [35] R. J. H. Clark, R. E. Hester, *Advances in Spectroscopy*, vol. 20, John Wiley & Sons, New York, **1993**.
- [36] H. Tang, H. Yao, G. Wang, Y. Q. Li, M. Feng, *Opt. Express* **2007**, *15*, 12708.
- [37] K. S. Kalasinsky, T. Hadfield, A. A. Shea, V. F. Kalasinsky, M. P. Nelson, J. Neiss, A. J. Drauch, G. S. Vanni, P. J. Treado, *Anal. Chem.* **2007**, *79*, 2658.

Supporting information

Additional supporting information may be found in the online version of this article at the publisher's web site.